

Reaching the intrinsic performance limits of superconducting strip photon detectors up to 0.1 mm wide

Kristen M. Parzuchowski^{1,2*}†, Eli Mueller^{1,3†},
 Bakhrom G. Oripov^{1,2}, Benedikt Hampel^{1,2},
 Ravin A. Chowdhury^{1,2}, Sahil R. Patel^{4,5}, Daniel Kuznesof⁶,
 Emma K. Batson^{1,7}, Ryan Morgenstern^{1,2}, Robert H. Hadfield⁶,
 Varun B. Verma¹, Matthew D. Shaw⁵, Jason P. Allmaras⁵,
 Martin J. Stevens¹, Alex Gurevich⁸, Adam N. McCaughan^{1,2}

¹National Institute of Standards and Technology, Boulder, CO, U.S.A.

²Department of Physics, University of Colorado, Boulder, CO, U.S.A.

³Department of Physics, University of Colorado, Denver, CO, U.S.A.

⁴Department of Applied Physics and Materials Science, California Institute of Technology, Pasadena, CA, U.S.A.

⁵Jet Propulsion Laboratory, California Institute of Technology, Pasadena, CA, U.S.A.

⁶James Watt School of Engineering, University of Glasgow, Glasgow, U.K.

⁷Department of Electrical Engineering and Computer Science, Massachusetts Institute of Technology, Cambridge, MA, U.S.A.

⁸Department of Physics, Old Dominion University, Norfolk, VA, U.S.A.

*Corresponding author(s). E-mail(s): kristen.parzuchowski@nist.gov;

Contributing authors: eli.mueller@nist.gov;

†These authors contributed equally to this work.

Abstract

Superconducting nanowire single-photon detectors (SNSPDs) have emerged as the highest performing photon-counting detectors, making them a critical technology in quantum photonics and photon-starved optical sensing. However, the

performance of SNSPDs is limited not by the intrinsic properties of the superconducting film, but by edge-induced current crowding. Despite extensive materials optimization and increasingly demanding fabrication strategies aimed at mitigating this edge-limited behavior, the device edges continue to limit the maximum device operating current, thereby degrading key performance metrics. Here, we demonstrate for the first time *in situ* tuning of a detector from an edge-limited to a bulk-limited regime, allowing the device to reach its intrinsic performance limit. Our approach is based on current-biased superconducting “rails” placed on either side of the detector to suppress current crowding at the edges. We show that activation of the rails reduces the dark count rate by nine orders of magnitude and extends the photon detection plateau at 1550 nm by more than 40%. These results are demonstrated on detectors up to 0.1 mm wide, establishing an entirely new class of ultra-wide strip detectors that we call superconducting strip photon detectors (SSPD). Moreover, the ability to suppress edge current crowding using the rails provides a pathway toward SSPDs with strip widths extending into the mm-scale. Such devices will enable large-area, high efficiency SSPD arrays with infrared sensitivity and open new opportunities in applications ranging from biomedical imaging [1] to deep space optical communication [2].

Introduction

State of the art SNSPDs now achieve detection efficiencies exceeding 98% [3, 4], dark count rates under 1 cnt/day [5], wire widths up to 20 μm [6, 7], and sensitivity extending into the mid-infrared [8, 9]. While these metrics are remarkable, they require specialized device designs that limit the ability of the device to optimize all these metrics simultaneously. In many cases, the breakthrough performance is obtained, directly or indirectly, by suppressing the contribution of edge-induced current crowding. However, these devices have yet to reach the intrinsic performance limit where edge-induced current crowding is eliminated and the dark counts are onset by the fundamental unbinding of vortex-antivortex (VAV) pairs. Accessing this regime would enable the simultaneous achievement of the optimal performance metrics of a given superconducting material.

The mechanism of edge current crowding is two-fold: First, real devices inevitably have lithographic defects along the edge of the strip, which lead to geometrical current crowding [10]. Second, the Meissner effect causes a non-uniform flow of sheet current density $J(x)$ across the strip width x , with $J(x)$ being lowest at the center and maximum at the edges. This intrinsic non-uniformity increases with the width of the strip w [11] and is generally seen as the fundamental barrier that prevents the development of SNSPDs with strip widths approaching the scale of the magnetic Pearl length Λ [12], typically on the order of 100’s of μm in thin-film SNSPD materials [11, 13].

The impact of this current crowding manifests in the maximum bias current at which the device can be operated. Although the theoretical upper bound on the total supercurrent is set by the depairing current I_d , the current crowding at the edge lowers the energy barrier for vortex entry at the device boundaries, causing the detector to switch to the normal state at a reduced current known as the switching current I_{sw} .

Even in state-of-the-art SNSPDs, the ratio $I_{\text{sw}}/I_{\text{d}}$, sometimes called the constriction factor, rarely exceeds 0.7 [14]. As a result, dark counts onset at relatively low operating currents, setting an extrinsic noise floor that is well above the intrinsic capabilities of the superconducting material. Further, this reduced I_{sw} has direct implications for photon detection: operating far below I_{d} increases the deposited photon energy per cross sectional area of the strip necessary to form a resistive hotspot, thereby enforcing the tradeoff between strip width and minimum detectable photon energy. In contrast, theoretical models predict that as I_{sw} approaches I_{d} , the minimum detectable photon energy becomes only weakly dependent on strip width [15], allowing the possibility to develop high efficiency SNSPDs with ultra-wide strip widths exceeding the Pearl length.

In this work, we introduce a method to *in situ* tune I_{sw} closer to I_{d} , thereby enabling the device to operate at its intrinsic performance limit. Our method relies on placing an SSPD between two current-carrying superconducting “rails”, as shown in Fig. 1(a). Here, the magnetic self-field of the rails partly cancels the perpendicular component of the self-field of the SSPD, reducing the current crowding at the edges [16, 17]. This results in a redistribution of the current density $J(x)$ that inverts the profile – yielding a minimum at the edges and maximum at the center. Figure 1(c) shows the evolution of $J(x)$ calculated by solving the London equation for different rail currents I_{r} (see supplementary information). The SSPD-rail architecture not only eliminates the edge current crowding relative to that of a bare SSPD without rails, but also allows *in situ* tuning of $J(x)$ at the edge by varying I_{r} to optimize the SSPD performance. This novel approach offers a principal opportunity to break the Pearl limit and develop high-performance SSPDs with $w > \Lambda$. For instance, Fig. S2 in the supplementary information shows tunable $J(x)$ profiles calculated for a 3 nm thick and 2.5 mm-wide WSi strip that is 4 times larger than Λ .

Here, we present experimental results on a variety of SSPD-rail devices composed of thin-film WSi ($\Lambda \approx 600 \mu\text{m}$) SSPDs with adjacent Nb rails. By turning on the rails, we demonstrate a 100 μm -wide SSPD with an over 9 orders of magnitude (extrapolated) reduction in dark counts and a detection plateau at 1550 nm widened by more than $\sim 40\%$. In a 20 μm -wide SSPD, we reached near unity internal detection efficiency (IDE) of 4 μm photons and lowered detector jitter by $\approx 30\%$. Furthermore, the rails allowed us to recover a detection plateau at 1550 nm in a device that would otherwise not be photosensitive because of its low $I_{\text{sw}}/I_{\text{d}}$ ratio. These significant improvements were made without compromising the photon detection efficiency across the width of the SSPD. Our results show that the rails tune the device performance from an edge-limited to a bulk-limited regime. To our knowledge, this is the first demonstration of *in situ* tuning of an SSPD to its intrinsic performance limit and establishes a pathway to scaling SSPDs to widths exceeding the Pearl length.

Results

Our SSPD-rail architecture is illustrated in Figure 1(a). An SEM image of a fabricated 50 μm -wide WSi SSPD with 4 μm -wide adjacent Nb rails is shown in Figure 1(b). Here the ≈ 50 nm-thick rails are displaced ≈ 150 nm from the edge of the SSPD.

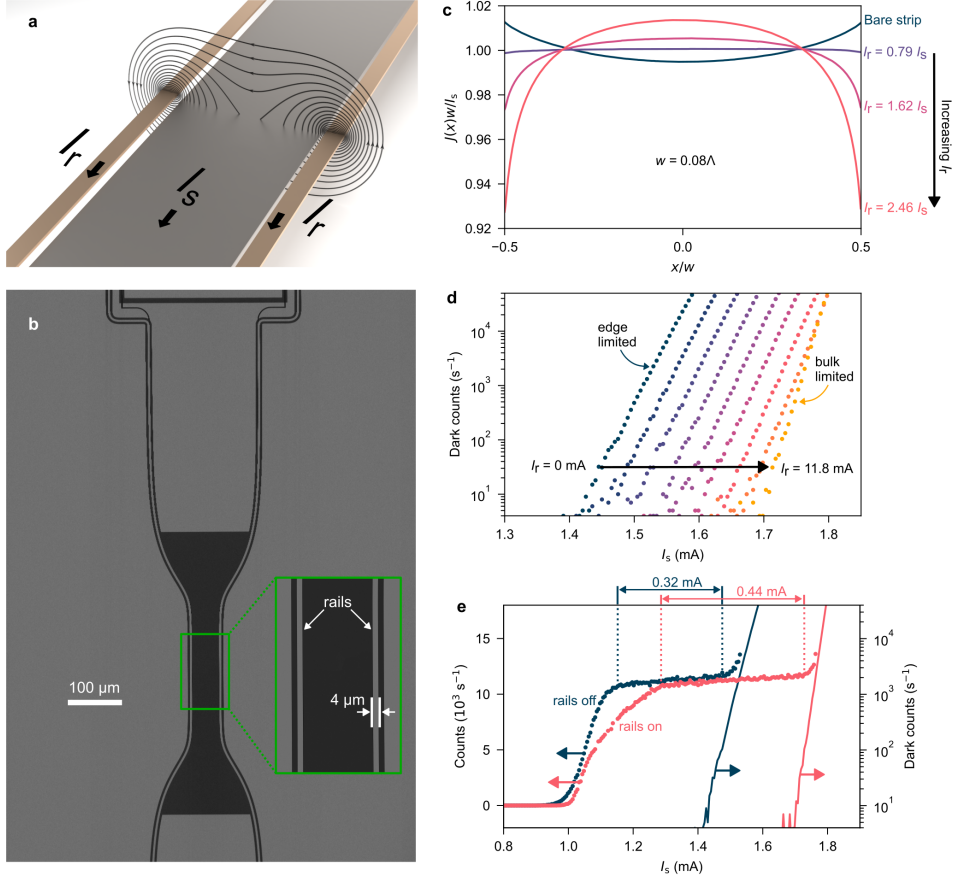


Fig. 1 (a) Illustration of SSPD (gray) integrated with adjacent rails (gold). The rails are displaced slightly from the edge of the strip. Simulated magnetic field lines are shown to demonstrate how the rails modify the self-induced magnetic field of the SSPD. (b) SEM image of 50 μm -wide WSi strip with 4 μm -wide Nb rails. The inset shows a zoomed-in image of the constriction. (c) Normalized current density as a function of position x along the wire width w simulated for a bare strip without rails (dark blue) and for a strip tuned by a series of increasing rail currents (purple to pink). For these simulations, the strip width is $w = 0.08\Lambda$ and the rails are displaced from the edges of the strip horizontally and vertically by $w/200$. (d) Measured dark count rate as a function of I_s on a 50 μm -wide strip for a series of increasing I_r values from 0 mA (dark blue) to 11.8 mA (yellow). Dark count rates onset at higher I_s as I_r is increased. (e) Measured 1550 nm photon count rate (left vertical axis, data points) and dark count rate (right vertical log-scale axis, lines) as a function of I_s for rails off (dark blue) and rails on (pink) for a 50 μm -wide strip. Gold covers were placed over the tapers of the SSPD to prevent detection events outside the constriction, as the measurements were performed under flood illumination. The plateau width is $\approx 320 \mu\text{A}$ with rails turned off and extends to $\approx 450 \mu\text{A}$ with rails turned on. The start of the plateau was set as the value of I_s at which the count rate exceeds $10.7 \times 10^3 \text{ s}^{-1}$. The end of the plateau was set as the value at which the dark count rate exceeds 100 s^{-1} .

The ≈ 3 nm-thick WSi strip has a constriction length of 100 μm . We fabricated (see details in Methods) and tested numerous devices varying in SSPD width from 1 μm to 100 μm . Here we present representative experimental results from these devices.

Suppression of dark counts

Figure 1(d) shows the dark count rate as a function of the SSPD bias current I_s for a series of I_r values for a 50 μm -wide strip. The dark count rate follows a log-linear dependence on I_s , consistent with dark counts initiated by Arrhenius thermally-activated vortex crossings [18] as described in the supplementary information. Increasing I_r from 0 mA up to 11.8 mA shifts the dark count rate curve to higher I_s values. For $I_r > 11.8$ mA (not shown), this trend reverses and the curve shifts to lower I_s . Here, $I_r^* = 11.8$ mA represents the optimal rail current that maximizes I_{sw} of the SSPD, defined operationally as the value of I_s at which the dark count rate exceeds 100 s^{-1} . The integration time for this measurement was 1 s, which limits the minimum measurable dark count rate to 1 s^{-1} . We extrapolated the I_r^* dark count curve to the I_s value at which the dark counts are 1000 s^{-1} for $I_r = 0$ and estimate a more than 8 orders of magnitude reduction in dark counts at I_r^* relative to $I_r = 0$. At $I_r \approx I_r^*$, there is an abrupt increase in the slope of the dark count rate curve that persists for $I_r > I_r^*$. As will be discussed below, this slope increase is indicative of a transition from a regime where dark counts are dominated by penetration of vortices from the edges ($I_r < I_r^*$), to a regime where dark counts are dominated by unbinding of VAV pairs in the bulk ($I_r > I_r^*$).

Rails impact on photosensitivity

Figure 1(e) shows the count rate as a function of I_s of the same 50 μm -wide device under flood illumination of $\lambda = 1550$ nm light with the rails off ($I_r = 0$ mA) and with the rails on ($I_r = I_r^*$). The count rate reaches a detection plateau, indicating saturated IDE, both with the rails on and off. Note that with the rails on, the onset of photosensitivity shifts to higher I_s compared to that with the rails off; however, the dark count onset shifts by an even larger amount, resulting in a $\approx 40\%$ increase in the detection plateau length.

Similarly, Fig 2(a) shows the count rate as a function of I_s for a 100 μm -wide device under flood illumination of $\lambda = 1550$ nm light with the rails off ($I_r = 0$ mA) and with the rails on ($I_r = I_r^*$). The count rate exhibits a slope on the plateau, which we attribute to photon detection events in the taper of the device. In contrast, the plateau in Fig. 1(e) is flat, as the tapers in that device were blocked with a gold layer. Similar to Fig. 1(e), turning the rails on shifts the onset of photosensitivity to higher I_s , while the dark-count onset shifts by a larger amount, resulting in a $\approx 43\%$ increase in the detection plateau length. We extrapolated the I_r^* dark count curve to the I_s value at which the dark counts are 1000 s^{-1} for $I_r = 0$ and estimate a more than 9 orders of magnitude reduction in dark counts at I_r^* relative to $I_r = 0$.

To test the upper bound on the wavelength sensitivity of our SSPD-rail devices, we tested a 20 μm -wide SSPD in a 300 mK cryostat [9] fit with an optical window for free-space coupled infrared light sources, which in this case was a blackbody source, and a monochromator at the 40 K stage for precise wavelength selection. This optical window resulted in higher background photon counts than for measurements performed at 1550 nm [Fig. 1(d) and Fig. 2(a)], which was done with a windowless 900 mK cryostat and a fiber-coupled laser. Figure 2(b) shows the measured photon count rate of the

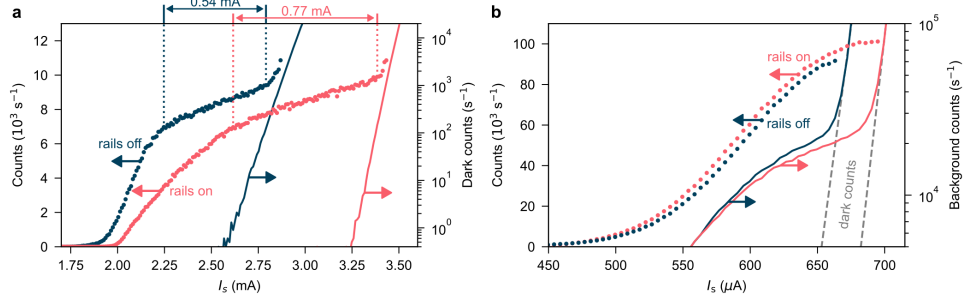


Fig. 2 (a) Measured flood-illuminated 1550 nm photon count rate (left vertical axis, data points) or dark count rate (right vertical log-scale axis, lines) as a function of I_s for rails off (dark blue) or rails on (pink) for a 100 μm -wide strip. The plateau width is $\approx 540 \mu\text{A}$ with rails turned off and extends to $\approx 770 \mu\text{A}$ with rails turned on. The start of the plateau was set as the value of I_s at which the count rate exceeds $6.9 \times 10^3 \text{ s}^{-1}$. The end of the plateau was set as the value at which the dark count rate exceeds 100 s^{-1} . (b) Measured flood-illuminated 4 μm photon count rate (left vertical axis, data points) and background count rate (right vertical log-scale axis, lines) on a 20 μm -wide strip as a function of I_s for rails off (dark blue) and rails on (pink). At low I_s the background counts are dominated by blackbody background photons entering through the free-space coupled cryostat, then, as I_s is increased, the exponential dark counts takeover as indicated by the dashed gray line. Turning on the rails shifts the dark counts to higher I_s enabling measurements at higher I_s . In this region, a rollover of counts is observed, indicating the start of a plateau and near unity IDE.

20 μm -wide SSPD under flood illumination of $\lambda = 4 \mu\text{m}$ photons as a function of I_s with the rails off ($I_r = 0 \text{ mA}$) and with the rails on ($I_r = I_r^*$). The background characteristic of this light source and cryostat is evident in the $I_s = 550 \mu\text{A}$ to $675 \mu\text{A}$ range before the log-linear dark counts dominate. By turning on the rails, the dark counts are reduced enabling measurement of the 20 μm -wide strip's photon count rate at higher I_s . The count rate at higher I_s increases and rolls over onto the start of a detection plateau, indicating near unity IDE.

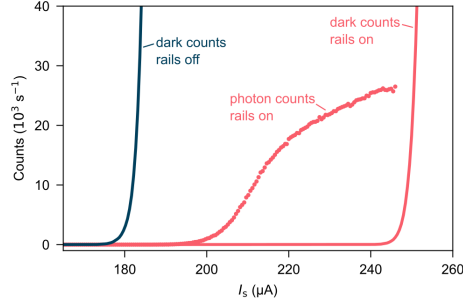


Fig. 3 Measured flood-illuminated 1550 nm photon count rate (pink data points) and dark count rate (lines) as a function of I_s for rails off (dark blue) and rails on (pink) on a 10 μm -wide strip with low I_{sw}/I_d ratio. With the rails off, the dark counts begin to dominate at such a low I_s that photon counts cannot be measured. With the rails on, a huge shift of dark counts to higher I_s is observed, and photon counts are measured with near unity IDE. The slope on the plateau is consistent with photon detection events in the taper of the device.

We also tested several 10 μm -wide SSPDs that showed unusually low $I_{\text{sw}}/I_{\text{d}}$ ratios, which we attribute to a higher prevalence of lithographic defects in this subset of devices. In Fig. 3, the measured flood-illuminated 1550 nm photon count rate and dark count rate is plotted as a function of I_{s} for one of these devices. With the rails off ($I_{\text{r}} = 0 \text{ mA}$), $I_{\text{sw}}/I_{\text{d}} \approx 44\%$ and the dark counts dominate at such a low I_{s} that the strip has no photosensitivity to 1550 nm photons. With the rails on ($I_{\text{r}} = 20.9 \text{ mA}$), the dark count curve shifts dramatically to higher I_{s} , reaching $I_{\text{sw}}/I_{\text{d}} \approx 63\%$, and photon counts can be measured with near unity IDE. Thus, the rails recovered the performance of the SSPD that otherwise would have been non-functional at 1550 nm.

Rails impact on timing jitter

Figure 4(a) shows the histogram of detection latency of a 20 μm -wide strip under 1550 nm flood illumination for six I_{r} values ranging from $I_{\text{r}} = 0$ to $I_{\text{r}} = 8.8 \text{ mA}$. The long tail is likely due to detection events in the taper of our strips as has been noted in previous studies [19]. As I_{r} is increased, the histogram narrows. We suspect that this may be caused by the merging of two latency distributions: one originating from edge vortex-mediated detections and another from bulk VAV-pair-mediated detections, however a more thorough study is necessary to confirm this.

In Fig. 4(b) the full width at half-maximum (FWHM) jitter is plotted as a function of I_{r} for several devices ranging from 5 μm to 20 μm in width. There is no clear dependence of jitter on strip width; however, all strips demonstrated improved jitter upon application of rail current until an optimum value is reached. This optimum jitter value typically occurred at an I_{r} that differed from I_{r}^* by a few milliamperes. After this optimum jitter value, the jitter slightly increases with added rail current. Interestingly, the optimum jitter of all three strip widths is similar, $\approx 35 \text{ ps}$. We estimate the longitudinal geometric jitter of these devices to be 34.3 ps, 27.1 ps and 21.2 ps for the 5 μm , 10 μm and 20 μm -wide devices, respectively. Further study is required to estimate the total geometric jitter.

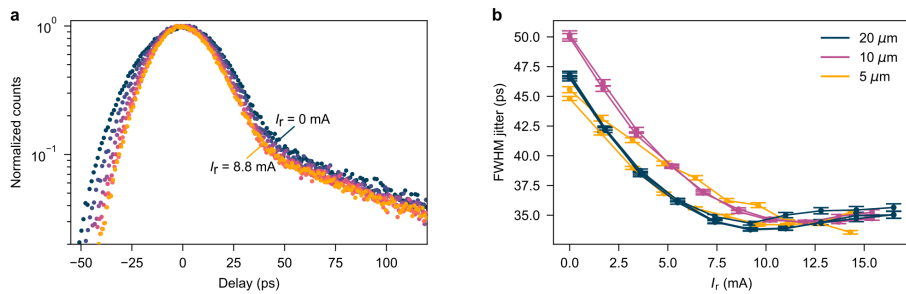


Fig. 4 (a) Jitter histograms for a 20 μm -wide strip under 1550 nm flood illumination for six equally-spaced I_{r} values ranging from $I_{\text{r}} = 0$ to $I_{\text{r}} = 8.8 \text{ mA}$. The long tail in the distribution for delay times greater than $\sim 50 \text{ ps}$ is likely due to detection events in the taper as these measurements were performed under flood illumination. The jitter histogram narrows as I_{r} is increased. (b) FWHM jitter as a function of I_{r} for two 5 μm (yellow), two 10 μm (pink) and three 20 μm (dark blue) wide strips. As I_{r} is increased, the jitter decreases until it reaches a minimum.

Tunable proximity to the depairing current

As a demonstration of how the rails increase the switching current, Fig. 5 shows $I_{\text{sw}}/I_{\text{d}}$ as a function of I_{r} for 20 μm , 50 μm , and 100 μm -wide devices. Here I_{sw} is defined as the value of I_{s} at which the dark count rate exceeds 100 s^{-1} . For all strip widths, $I_{\text{sw}}/I_{\text{d}}$ increases for positive I_{r} and reaches a peak over the range of I_{r} measured. This peak occurs at I_{r}^* . As strip width increases, the change in $I_{\text{sw}}/I_{\text{d}}$ with I_{r} becomes more significant. This trend is consistent with our calculations that show that wider strips with correspondingly stronger edge current crowding benefit more from its suppression by the rails.

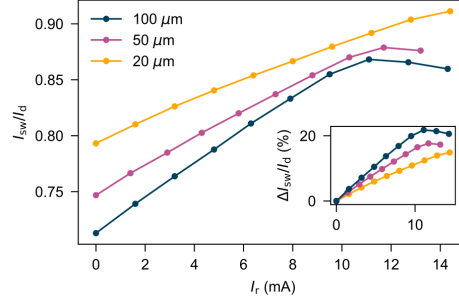


Fig. 5 Measured $I_{\text{sw}}/I_{\text{d}}$ as a function of I_{r} for strip widths of 20 μm (yellow), 50 μm (pink) and 100 μm (dark blue). As I_{r} is increased, $I_{\text{sw}}/I_{\text{d}}$ also increases until it reaches I_{r}^* . Change (Δ) in $I_{\text{sw}}/I_{\text{d}}$ as a function of I_{r} is shown in the inset for the same devices. As wire width is increased, larger increases in $I_{\text{sw}}/I_{\text{d}}$ are measured.

To determine the depairing current of our film, which was used in Fig. 5, we measured the change in kinetic inductance of step-impedance resonators as a function of bias current as described in Ref. [14]. These resonators were fabricated from a nominally identical film to that used for the SSPD-rail devices. The measured kinetic inductance change was fit to the fast and slow relaxation models described in Ref. [20]. We found that the fast relaxation model was a better fit for all resonators. These fits were used to derive the depairing current with an average of $39 \mu\text{A} \mu\text{m}^{-1}$.

Discussion

Our results show that SSPD-rail devices reverse current crowding at the strip edges and remove the fundamental Pearl length limitation on strip width. This also follows from our numerical calculations that show that the current density at the edges can be reduced lower than that in the center of the strip even for a SSPD with $w \gg \Lambda$. Moreover, the required reduction of $J(x)$ at the edges is achieved with a normalized rail current $I_{\text{r}}/I_{\text{s}}$ that diminishes as the strip width increases from $w \ll \Lambda$ to $w > \Lambda$. We anticipate that the next limitation to scale to wider SSPD widths may be set by a degradation in film quality over large length scales.

We observed that for all devices with $w \geq 5 \mu\text{m}$, $I_{\text{sw}}(w)$ is maximized at optimum rail currents $I_{\text{r}}^*(w)$. The slopes of the log-linear dark count rates as a function of I_{s}

(such as that shown in Fig. 1(d)) increase abruptly at $I_r = I_r^*$. The dark count rate S generally follows a thermally-activated Arrhenius behavior caused by penetration of vortices from the edge given by $S_e(I_s) \simeq S_{e0} \exp[-(1 - I_s/I_d)U_e/T]$ where U_e is the energy barrier for vortex entry. For the data $I_r < I_r^*$, we have $U_e \approx 83\text{ K}$ for the $50\text{ }\mu\text{m}$ -wide strip shown in Fig. 1(d) and $U_e \approx 71\text{ K}$ for the $100\text{ }\mu\text{m}$ -wide strip shown in Fig. 2(a). These values of U_e are consistent with our evaluation of the vortex energy barrier for penetration of vortices from the edges given in the supplementary information. In turn, the nearly doubling of the logarithmic slope observed at $I_r > I_r^*$ is strong experimental evidence that the dark count rate becomes dominated by the unbinding of VAV pairs of radius $\sim \xi J_d/J \ll w$ in the center of the strip. This is because the energy of a vortex spaced by u from an ideal edge of a strip is half the energy of a VAV pair of radius u in the bulk of a strip, so that now the dark count rate is given by $S_b(I) \simeq S_{b0} \exp[-(1 - I_s/I_d)U_b/T]$ where $U_b = 2U_e$.

As shown in the supplementary information, the ratio of the logarithmic slopes $\partial_{I_s} \ln S$ for vortex hopping from the edges and for bulk VAV pair production are related by $\partial_{I_s} \ln S_b / \partial_{I_s} \ln S_e \simeq 2\tilde{J}_d/J_d$ where J_d and \tilde{J}_d are the mean depairing current densities in the bulk and at the edges, respectively. Here \tilde{J}_d is reduced relative to J_d by the current crowding at lithographic defects. For instance, the slope ratio ≈ 1.79 observed in the $50\text{ }\mu\text{m}$ -wide strip shown in Fig. 1(d) implies $\tilde{J}_d = 0.895J_d$ and the ratio ≈ 1.53 observed in the $100\text{ }\mu\text{m}$ -wide strip shown in Fig. 2(a) implies $\tilde{J}_d = 0.765J_d$. To mitigate penetration of vortices from the edges for these strips, the rails should carry current sufficient to reduce $J(x)$ at the edges by 10.5% and 23.5% respectively, which is consistent with our numerical results shown in the supplementary information.

Two important conclusions follow from our analysis of dark counts: (1) In addition to increasing I_{sw} , the rails greatly (up to 9 orders of magnitude) reduce dark counts caused by penetration of vortices from the edges. (2) At $I_r = I_r^*$ the strip achieves its maximum I_{sw}/I_d . As stated above, we define I_{sw} as the current at which the dark count rate equals 100 s^{-1} . The VAV pair unbinding makes it impossible to reach $I_s = I_d$ in a strip without switching to the normal state, but, the rails do allow the device to operate at its intrinsic performance limit. In addition to the fundamental limits of I_{sw} and the SSPD sensitivity, which are both caused by the bulk VAV pair production evaluated in the supplementary information, there are also technological and materials science limitations to its maximum value. These limitations result from variations in film thickness, lithographic defects, inhomogeneities of superconducting properties due to local non-stoichiometry, grain boundaries in polycrystalline films, film adhesion with the substrate, etc. Beyond these limitations, our estimated I_d has uncertainty associated with it. For example, our method for estimating I_d of our devices uses assumptions from the BCS model, which do not account for the effects of strong electron-phonon pairing of the Eliashberg theory [21], or the reduction of J_d by subgap quasiparticle states [22] which are especially pronounced in thin superconducting films. Nonetheless, tuning $J(x)$ by rails enables reaching the operational limit of I_{sw} for a particular SSPD even if both the exact value of J_d and the extent of reduction of J_d at the edges is unknown.

We observed that current redistribution in SSPDs was possible without affecting detection efficiency uniformity; the photon count rate on the detection plateau

varies by less than 1% across the full range of I_r as described in the Methods section. However, the results shown in Fig. 1(e) and Fig. 2(a) clearly show that the onset of photosensitivity shifts slightly to higher I_s with the rails on. This behavior may reflect a nonuniform threshold current density for photodetection across the strip in which the photon detections near the edge have a lower detection threshold current density than that in the bulk [23–25]. In this scenario, when the rails are turned off, the edges will become photosensitive at a lower I_s relative to that for the bulk. However, when the rails are turned on and the current density near the edges is reduced, a higher total I_s is required for the edge to reach the same threshold, shifting the onset of photosensitivity to higher I_s . We also observed a broadening of the photosensitivity onset with the rails turned on. This may be consistent with a new nonuniform threshold current-density profile. However, several mechanisms are known to influence the functional form of the IDE as a function of I_s [26], and distinguishing among the possible mechanisms is beyond the scope of this work.

Turning to the timing jitter observed in our devices, the ≈ 50 ps jitter on our devices up to $20\ \mu\text{m}$ wide warrants further discussion. This result seems inconsistent with models in which components of the VAV pair generated by a photon near the edge and in the center of the strip have different transit times [15] so that wider strips would have greater timing jitter. This model, along with previous experiments studying jitter dependence on strip width [19] have primarily focused on nanostrips ≈ 100 nm wide. It remains unclear how the jitter scales as the widths increase to $1\ \mu\text{m}$ - $100\ \mu\text{m}$. For instance, taking the terminal velocity of a vortex $v_c \simeq 20\ \text{km s}^{-1}$ measured on Pb film bridges [27] at $J \approx J_d$, one would expect a jitter $\sim w/v_c \sim 1\ \text{ns}$ in a $20\ \mu\text{m}$ -wide strip, which is 20 times larger than the observed jitter of $\sim 50\ \text{ps}$ shown in Fig. 4. The value of v_c observed on Pb is qualitatively consistent with the estimate $v_c \simeq J_d/\eta \simeq \rho_n \xi / 2\mu_0 \lambda^2$, where $\eta = \phi_0^2 / 2\pi \xi^2 \rho_n$ is the Bardeen–Stephen vortex drag coefficient, ρ_n is a normal-state resistivity at T_c , and $J_d \simeq \phi_0 / 4\pi \mu_0 \lambda^2 \xi$. The same estimate of v_c for our WSi film with $\xi = 10\ \text{nm}$, $\lambda = 950\ \text{nm}$ and $\rho_n = 2.5\ \mu\Omega \cdot \text{m}$ yields $v_c \sim \rho_n \xi / 2\mu_0 \lambda^2 \sim 11\ \text{km s}^{-1}$, which again predicts a jitter substantially larger than that observed on the $20\ \mu\text{m}$ -wide SSPD. Thus, real devices significantly outperform the estimates of conventional models of vortex-assisted jitter, showing that our current understanding of the dynamics of a resistive domain produced by photon absorption is still incomplete.

It is worth noting that the ultra-wide SSPDs studied here showed broad detection plateaus for $1550\ \text{nm}$ photons even without applying rail current. In addition, a control device without rails, or otherwise any Nb nearby, also demonstrated a similar detection plateau, indicating that the rail structures are not required for high efficiency photosensitivity to $1550\ \text{nm}$ photons. This result is remarkable, and we attribute this to two factors: (1) our fabrication process which minimized the likelihood for lithographic defects and (2) our choice of SSPD material. To the former point, our SSPDs were fabricated using electron-beam lithography and designed with relatively short strip lengths, both of which help minimize the number of edge defects [28] and resulted in a fairly high I_{sw}/I_d compared to those noted in previous works [11, 14, 29]. To the latter point, our detector material is a highly uniform amorphous superconductor [30] and the thin film WSi recipe has a high silicon content (≈ 0.48 Si mole fraction) designed

to maximize photosensitivity in wide strips [29]. We also note that our strips do not self reset without shunting the device with an inductor and resistor in parallel with the SSPD at low temperature. This behavior is likely generic to ultra-wide SSPDs and may have caused wide strips to be overlooked in the past.

In two recent works by Miki and coworkers [6, 7], SSPDs of width $20\ \mu\text{m}$ ($18\ \mu\text{m}$ -wide active area) made from NbTiN thin-films were demonstrated. In this study, the authors used a “high-critical current bank (HCCB)” structure, in which the center of the strip material is irradiated with ions to selectively lower I_d relative to the edges. For a fixed current flowing through the strip, this irradiation allows the center, the photoreceiving area, to operate closer to I_d than without irradiation. This approach demonstrated unity IDE at $2\ \mu\text{m}$ for the $20\ \mu\text{m}$ -wide strip. However, the HCCB does not suppress the edge current crowding caused by the Pearl length, and instead partially compensates for it by reducing I_d in the center relative to the edges. If the strip width continues to approach and exceed the Pearl length, the current crowding will continue to grow and eventually exceed the additional vortex energy barrier provided by the HCCB. Therefore, the fundamental limitation on the maximum size of strip width achievable using this approach is still limited by the Pearl length.

Finally, in addition to boosting the performance limits of any given SSPD, the rails can also help resolve the Berezinskii–Kosterlitz–Thouless (BKT) transition in thin films [31]. As pointed out above, the abrupt change in the slope of the dark count rate at the optimum rail current I_r^* shown in Fig. 1(d) is a clear experimental indication of the suppression of single-vortex penetration from the edges and a transition to BKT unbinding of VAV pairs inside the film. Thus, using rails can be helpful in fundamental investigations of the BKT transition without the masking effects of edge-induced vortex entry.

Conclusion

We have demonstrated, for the first time, a method to tune the performance of an SSPD to its intrinsic limits, paving the way to scale to strip widths exceeding the Pearl length. The approach uses current-biased superconducting rails on each side of the strip to reduce the current density at the edges, allowing the device to operate at a higher fraction of the depairing current. We pushed the performance of a $100\ \mu\text{m}$ -wide SSPD to its intrinsic performance limit, demonstrating an extension of the detection plateau at $1550\ \text{nm}$ and over 9 orders-of-magnitude reduction in dark counts. This detector well surpasses the widest reported SSPDs which are $20\ \mu\text{m}$ wide [6, 7]. We demonstrated that rails provide numerous other follow-on performance benefits to SSPD technology including increased upper bound of wavelength sensitivity, recovery of detector functionality in low performing devices, and improved detector jitter.

The orders-of-magnitude reduction in dark counts has positive follow-on consequences for scaling these detectors into arrays. In an array the total dark count rate is multiplied by the number of individual detectors, and thus can quickly add up to a sizeable number of dark counts [32]. With rails, the dark counts can easily be reduced to a nearly negligible rate.

The ability to scale to wide strips is important and previously was inaccessible. Wide strips eliminate the need to meander a detector to create a high fill factor [33]. With a focused beam, all of the photons of interest can be collected onto our $100\text{ }\mu\text{m}$ -wide detector. Scaling these wide strips up into arrays, the fill factor can be much higher than previous demonstrations [32]. Furthermore, meandered detectors are sensitive to the polarization of light, with light polarized parallel to the straight sections of the detector being less efficiently detected. In the case of our wide detectors, all polarizations are detected with equal efficiency.

In future studies, we foresee being able to scale these detectors to widths wider than the Pearl length, which could yield high efficiency free-space coupled SSPDs – eliminating the need for lossy fiber optics. These detector could immediately be applied to quantum information experiments where loss is detrimental to the fidelity of the transmitted quantum state.

Acknowledgements. This research was funded by NIST (<https://ror.org/05xpvk416>), University of Colorado Boulder (<https://ror.org/02ttsq026>), and the DARPA DSO Synthetic Quantum Nanostructures program. The U.S. Government is authorized to reproduce and distribute reprints for governmental purposes notwithstanding any copyright annotation thereon. DK thanks the EPSRC and SFI Centre for Doctoral Training in Photonic Integration for Advanced Data Storage (CDT-PIADS EP/S023321/1).

Methods

Fabrication

The chips were fabricated with 5 layers: 1 WSi layer, 1 Nb layer, 1 Au layer and 2 dielectric (SiO_2) spacer layers. First, we sputter a $\approx 3\text{ nm}$ -thick film of WSi on a 75 mm silicon wafer with 150 nm of thermal oxide. The film was capped with $\approx 2\text{ nm}$ αSi to prevent oxidation. Next we patterned our strips using ZEP520A using electron-beam lithography. Then the film was etched using an inductively coupled plasma-reactive ion etcher (ICP-RIE) and an AR:SF6 etch.

For the next layer, we pattern LOR3A + SPR660 using photolithography for the dielectric spacer layer. We sputter $\approx 25\text{ nm}$ SiO_2 and liftoff the resist – this layer isolates the WSi strip from the Nb rails. Then, we pattern LOR3A + SPR660 using photolithography for Nb liftoff. We then sputter $\approx 100\text{ nm}$ of Nb and lift it off. Next, we pattern our rails using ZEP520A using electron-beam lithography. The Nb is etched using the ICP etcher and an SF6 etch.

For the next layer, we pattern LOR3A + SPR660 using photolithography for the dielectric spacer layer. We sputter $\approx 25\text{ nm}$ SiO_2 and liftoff the resist – this layer isolates the Nb rails from the Au covers. Then we pattern taper covers in LOR3A + SPR660 using photolithography for Au liftoff. We evaporate $\approx 100\text{ nm}$ Au and lift it off.

Verification of Unity Internal Detection Efficiency

As noted in Fig 2(a), a slope on our detection plateau was evident for uncovered detectors of all widths. We hypothesize that this slope is a result of our experiments being performed under flood illumination causing detection events in the taper of our devices as has been noted in previous studies [29]. To test this hypothesis, we fabricated several devices with gold covers placed over the taper in order to block light from hitting the tapers. In these gold covered devices, the only region exposed to light should be the uncovered portion of the constriction. In Fig 1(e) we show an example of results obtained using a $50\ \mu\text{m}$ device with a gold cover. The gold cover has a $10\ \mu\text{m}$ -long opening over the center of the constriction. Here the slope appears to be completely eliminated by the addition of the cover. In the case of the $100\ \mu\text{m}$ -wide SSPDs with gold covers, we do not measure a complete reduction in plateau slope. Further study is needed to determine the cause of this discrepancy.

We also verified unity internal detection efficiency using a focused beam spot on a $20\ \mu\text{m}$ -wide SSPD. Here we measured the photon count rate on the plateau as a function of rail current and found less than 1% variation in the count rate over the range of rail current studied here.

References

- [1] Wang, Q. *et al.* A comprehensive overview of diffuse correlation spectroscopy: theoretical framework, recent advances in hardware, analysis, and applications. *NeuroImage* **298**, 120793 (2024).
- [2] Wollman, E. E. *et al.* SNSPD-based detector system for nasa's deep space optical communications project. *Optics Express* **32**, 48185–48198 (2024).
- [3] Reddy, D. V., Nerem, R. R., Nam, S. W., Mirin, R. P. & Verma, V. B. Superconducting nanowire single-photon detectors with 98% system detection efficiency at 1550 nm. *Optica* **7**, 1649–1653 (2020).
- [4] Li, Z.-G. *et al.* Surpassing 99% detection efficiency by cascading two superconducting nanowires on one waveguide with self-calibration. *Light: Science & Applications* **14**, 369 (2025).
- [5] Chiles, J. *et al.* New constraints on dark photon dark matter with superconducting nanowire detectors in an optical haloscope. *Physical review letters* **128**, 231802 (2022).
- [6] Yabuno, M., China, F., Terai, H. & Miki, S. Superconducting wide strip photon detector with high critical current bank structure. *Optica Quantum* **1**, 26–34 (2023).
- [7] Yabuno, M., China, F., Terai, H. & Miki, S. Two-micron-wavelength single-photon detection using the high-critical-current-bank structure superconducting wide strip photon detector. *Optics Express* **33**, 24927–24936 (2025).

- [8] Taylor, G. G. *et al.* Low-noise single-photon counting superconducting nanowire detectors at infrared wavelengths up to 29 μm . *Optica* **10**, 1672–1678 (2023).
- [9] Hampel, B. *et al.* Tungsten germanide single-photon detectors with saturated internal detection efficiency at wavelengths up to 29 μm . *arXiv preprint arXiv:2511.20868* (2025).
- [10] Clem, J. R. & Berggren, K. K. Geometry-dependent critical currents in superconducting nanocircuits. *Physical Review B—Condensed Matter and Materials Physics* **84**, 174510 (2011).
- [11] Haneishi, T., Yabuno, M., Kutsuma, H., Miki, S. & Yamashita, T. Evaluation of NbTiN superconducting strip photon detectors with 0.1–30 μm strip widths. *IEEE Transactions on Applied Superconductivity* (2024).
- [12] Pearl, J. Current distribution in superconducting films carrying quantized fluxoids. *Applied Physics Letters* **5**, 65 (1964).
- [13] Zhang, X. *et al.* Characteristics of superconducting tungsten silicide $\text{W}_x\text{Si}_{1-x}$ for single photon detection. *Phys. Rev. B* **94**, 174509 (2016).
- [14] Frasca, S. *et al.* Determining the depairing current in superconducting nanowire single-photon detectors. *Physical Review B* **100**, 054520 (2019).
- [15] Vodolazov, D. Y. Single-photon detection by a dirty current-carrying superconducting strip based on the kinetic-equation approach. *Physical Review Applied* **7**, 034014 (2017).
- [16] Castellani, M. *et al.* A superconducting full-wave bridge rectifier. *Nature Electronics* 1–9 (2025).
- [17] Cadorm, L. R., Sardella, E. & Silva, C. C. d. S. Harnessing the superconducting diode effect through inhomogeneous magnetic fields. *Physical Review Applied* **21**, 054040 (2024).
- [18] Bulaevskii, L., Graf, M., Batista, C. & Kogan, V. Vortex-induced dissipation in narrow current-biased thin-film superconducting strips. *Physical Review B—Condensed Matter and Materials Physics* **83**, 144526 (2011).
- [19] Korzh, B. *et al.* Demonstration of sub-3 ps temporal resolution with a superconducting nanowire single-photon detector. *Nature Photonics* **14**, 250–255 (2020).
- [20] Clem, J. R. & Kogan, V. Kinetic impedance and depairing in thin and narrow superconducting films. *Physical Review B—Condensed Matter and Materials Physics* **86**, 174521 (2012).

- [21] Nicol, E. & Carbotte, J. Temperature dependence of the critical pair-breaking current in thin-film, strong-coupling superconductors. *Physical Review B* **43**, 10210 (1991).
- [22] Kubo, T. Superfluid flow in disordered superconductors with dynes pair-breaking scattering: Depairing current, kinetic inductance, and superheating field. *Physical Review Research* **2**, 033203 (2020).
- [23] Zotova, A. & Vodolazov, D. Y. Intrinsic detection efficiency of superconducting nanowire single photon detector in the modified hot spot model. *Superconductor Science and Technology* **27**, 125001 (2014).
- [24] Renema, J. J. *et al.* Position-dependent local detection efficiency in a nanowire superconducting single-photon detector. *Nano letters* **15**, 4541–4545 (2015).
- [25] Wang, Q., Renema, J. J., Engel, A., van Exter, M. P. & de Dood, M. J. Local detection efficiency of a NbN superconducting single photon detector explored by a scattering scanning near-field optical microscope. *Optics Express* **23**, 24873–24887 (2015).
- [26] Kozorezov, A. *et al.* Fano fluctuations in superconducting-nanowire single-photon detectors. *Physical Review B* **96**, 054507 (2017).
- [27] Embon, L. *et al.* Imaging of super-fast dynamics and flow instabilities of superconducting vortices. *Nature communications* **8**, 85 (2017).
- [28] Gaudio, R., Zhou, Z., Sahin, D., Fiore, A. *et al.* Inhomogeneous critical current in nanowire superconducting single-photon detectors. *Applied Physics Letters* **105** (2014).
- [29] Chiles, J. *et al.* Superconducting microwire detectors based on wsi with single-photon sensitivity in the near-infrared. *Applied Physics Letters* **116** (2020).
- [30] Marsili, F. *et al.* Detecting single infrared photons with 93% system efficiency. *Nature Photonics* **7**, 210–214 (2013).
- [31] Halperin, B. & Nelson, D. R. Resistive transition in superconducting films. *Journal of low temperature physics* **36**, 599–616 (1979).
- [32] Oripov, B. G. *et al.* A superconducting nanowire single-photon camera with 400,000 pixels. *Nature* **622**, 730–734 (2023).
- [33] Reddy, D. V., Otrrooshi, N., Nam, S. W., Mirin, R. P. & Verma, V. B. Broadband polarization insensitivity and high detection efficiency in high-fill-factor superconducting microwire single-photon detectors. *APL Photonics* **7** (2022).

Supplementary Information

Field and current in the rail SSPD

Consider a long thin film strip of width w situated at $y = 0$ between two thin film rails of width l at $w/2 + b < x < w/2 + b + l$ and $-w/2 - b - l < x < -w/2 - b$, as shown in Fig. S1. Here each rail is raised by the height h and spaced by b from the edge of the strip. It is assumed that the strip carries a dc current I_s and each rail carries a dc current I_r , both the strip and the rails are infinite along z .

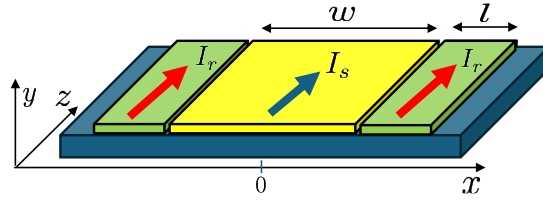


Fig. S1 Geometry of a detector film of width x and two current rails of width l . The coordinate axes are shifted downward for clarity.

In this geometry the z -component of magnetic field B_z along the strip vanishes and other field components $B_x = \partial A / \partial y$ and $B_y = -\partial A / \partial x$ are expressed in terms of the z component of the vector potential $\mathbf{A}(x, y) = [0, 0, A(x, y)]$ caused by currents flowing along z . Here $A(x, y)$ satisfies the London equation:

$$\lambda^2 \nabla^2 A - dQ(x)\delta(y) = 0, \quad (\text{S1})$$

where the gauge-invariant $\mathbf{Q} = \mathbf{A} + (\phi_0/2\pi)\nabla\theta$ is proportional to the supercurrent density $\mathbf{j} = -\mathbf{Q}/\mu_0\lambda^2$ in the film, θ is the phase of the superconducting order parameter, ϕ_0 is the magnetic flux quantum, λ is the London penetration depth, d is the film thickness. In the planar geometry considered here $j_x = j_y = 0$ and $j_z(x)$ flowing along the strip and the rails can depend only on x so the phase gradient $\nabla\theta = (0, 0, \theta')$ has only a constant z -component θ' independent of x . We consider here films with $d \ll \lambda$ in the absence of vortices and $Q \ll \phi_0/2\pi\xi$ for which the linear London electrodynamics is applicable, where ξ is a coherence length. Solution of Eq. (S1) is given by:

$$A(x, y) = \frac{d_s w}{8\pi\lambda_s^2} \int_{-1}^1 \ln[(x - u)^2 + y^2] Q_s(u) du + \quad (\text{S2})$$

$$\frac{d_r w}{8\pi\lambda_r^2} \left[\int_{1+b}^{1+b+l} \ln[(x-u)^2 + (y-h)^2] Q_r(u) du + \int_{-1-b-l}^{-1-b} \ln[(x-u)^2 + (y-h)^2] Q_r(u) du \right],$$

where $Q_s(x)$ and $Q_r(x)$ determine the supercurrent densities in the strip and the rails, respectively. Here λ_s and λ_r are the London penetration depths in the strip and the rail, d_s and d_r are their respective thicknesses, and all lengths are in units of $w/2$. Using $Q_s(u) = Q_s(-u)$ and $Q_r(u) = Q_r(-u)$ reduces Eq. (S2) to

$$A(x, y) = k_s \int_0^1 \ln[((x-u)^2 + y^2)((x+u)^2 + y^2)] Q_s(u) du + k_r \int_{1+b}^{1+b+l} \ln[((x-u)^2 + (y-h)^2)((x+u)^2 + (y-h)^2)] Q_r(u) du, \quad (\text{S3})$$

where $k_s = w/4\pi\Lambda_s$, $k_r = w/4\pi\Lambda_r$, and $\Lambda_s = 2\lambda_s^2/d_s$ and $\Lambda_r = 2\lambda_r^2/d_r$ are the Pearl screening lengths in the strip and rails, respectively. Setting $y = 0$ in Eq. (S3) and using $A(x, 0) = Q(x, 0) - \phi_0\theta'/2\pi$ gives two equations for $Q_s(x)$ and $Q_r(x)$:

$$Q_s(x) - 2k_s \int_0^1 \ln|x^2 - u^2| Q_s(u) du - k_r \int_{1+l}^{1+l+b} \ln[(u^2 + h^2 - x^2)^2 + 4h^2 x^2] Q_r(u) du = \alpha, \quad (\text{S4})$$

$$Q_r(x) - 2k_r \int_{1+b}^{1+b+l} \ln|x^2 - u^2| Q_r(u) du - k_s \int_0^1 \ln[(u^2 + h^2 - x^2)^2 + 4h^2 x^2] Q_s(u) du = \beta, \quad (\text{S5})$$

where $\alpha = \phi_0\theta'_s/2\pi$ and $\beta = \phi_0\theta'_r/2\pi$ with constant phase gradients θ'_s and θ'_r .

Equations (S4) and (S5) were solved numerically by discretizing $u_n = s(n-1)$, $n = 1, \dots, N_1$ and introducing a vector $Q = (Q_1, Q_2, \dots, Q_{N_1})$ which includes $Q_s(sn)$ at $1 < n < N$ and $Q_r(sn)$ at $N+1 < n < N_1$ with $s = 1/(N-1)$, $N_1 = [(1+l)N]$ and $N = 4 \cdot 10^3$. As a result, Eqs. (S4) and (S5) take the matrix form:

$$\sum_m M_{nm} Q_m = \alpha_n, \quad Q_n = \sum_m M_{nm}^{-1} \alpha_m. \quad (\text{S6})$$

Here M_{nm} defined by Eqs. (S4) and (S5) is given below, $\alpha_n = \alpha$ at $1 < n < N$, $\alpha_n = \beta$ at $N+1 < n < N_1$. To express α and β in terms of currents $I_s = (4s/\mu_0\Lambda_s) \sum_{n=1}^N Q_n$ and $I_r = (2s/\mu_0\Lambda_r) \sum_{n=N+1}^{N_1} Q_n$, we sum up the second Eq. (S6) over n using that α_m are constants at $1 < m < N$ and $N+1 < m < N_1$ and obtain:

$$I_s = A\alpha + B\beta, \quad I_r = A_1\beta + B_1\alpha, \quad (\text{S7})$$

Hence,

$$\alpha = \frac{A_1 I_s - B I_r}{A A_1 - B B_1}, \quad \beta = \frac{A I_r - B_1 I_s}{A A_1 - B B_1}, \quad (\text{S8})$$

where

$$A = \frac{4s}{\mu_0 \Lambda_s} \sum_{n=0}^N \sum_{m=0}^N M_{nm}^{-1}, \quad B = \frac{4s}{\mu_0 \Lambda_s} \sum_{n=0}^N \sum_{m=N+1}^{N_1} M_{nm}^{-1}, \quad (\text{S9})$$

$$A_1 = \frac{2s}{\mu_0 \Lambda_r} \sum_{n=N+1}^{N_1} \sum_{m=N+1}^{N_1} M_{nm}^{-1}, \quad B_1 = \frac{2s}{\mu_0 \Lambda_r} \sum_{n=0}^N \sum_{m=N+1}^{N_1} M_{nm}^{-1} \quad (\text{S10})$$

The matrix elements M_{nm} are given by

$$\begin{aligned} M_{nm} &= \delta_{nm} - 2k_s s \ln |(n^2 - m^2)s^2|, \quad 0 < n < N, \quad 1 < m < N, \\ M_{nm} &= -k_r s \ln[((m^2 - n^2)s^2 + h^2)^2 + (2hns)^2], \quad 0 < n < N, \quad N+1 < m < N_1, \\ M_{nm} &= -k_r s \ln[((m^2 - n^2)s^2 + h^2)^2 + (2hns)^2], \quad N+1 < n < N_1, \quad 1 < m < N, \\ M_{nm} &= \delta_{nm} - 2k_r s \ln |(n^2 - m^2)s^2|, \quad N+1 < n < N_1, \quad N+1 < m < N_1. \end{aligned}$$

The reduction of the sheet current density $J(x) = dj(x)$ at the edges by the magnetic field produced by rails comes from off-diagonal elements of M_{nm} accounting for the inductive coupling of rails and SSPD. Examples $J(x)$ in strips of different widths calculated from Eqs. (S4) and (S5) are shown in Fig. 1(a) in the main text and Fig. S2. Particularly, Fig. S2(b) shows that a nearly flat $J(x)$ profile with the rail-controlled reduction of $J(x)$ at the edges can be obtained in a strip 4 times wider than the Pearl length. For $\Lambda \approx 600 \mu\text{m}$ for our WSi films, Fig. S2(b) corresponds to a 2.4 mm wide strip. After $Q_s(x)$ and $Q_r(x)$ have been obtained, the magnetic field around the SSPD-rail is calculated using Eq. (S2), as shown in Fig. 1(a) in the main text.

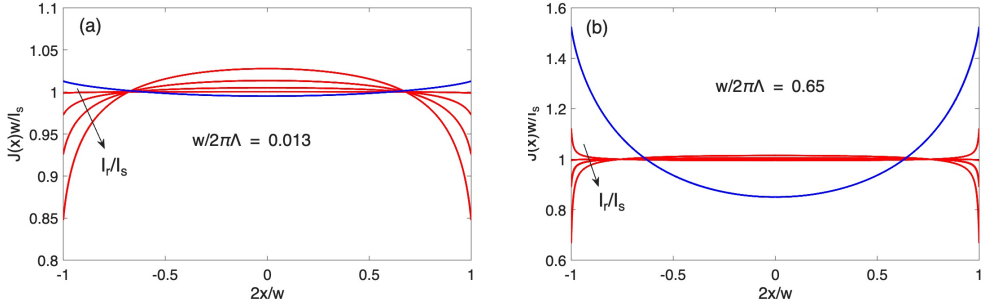


Fig. S2 Sheet current density $J(x)$ calculated for different film widths w and normalized rail currents I_r/I_s for the parameters of WSi films with $d_s = 3 \text{ nm}$, $\Lambda_s = 602 \mu\text{m}$, $k_r = 200k_s$ and $l = 0.15w$: (a) $w \approx 50 \mu\text{m}$, $I_r/I_s = 2.5, 5.03, 7.58, 10.12$, (b) $w \approx 2.5 \text{ mm}$, $I_r/I_s = 0.64, 0.82, 1.01, 1.21$.

Energy barriers and dark count rates caused by vortices

The position-dependent energy of a vortex $E(x)$ in a thin film of width $w \ll \Lambda_s$ calculated in the London model is given by [1]:

$$E(x) = \epsilon \ln \left(\frac{w}{\pi \tilde{\xi}} \sin \frac{\pi x}{w} \right) - \phi_0 J_s x, \quad (\text{S11})$$

where $\epsilon = \phi_0^2 / 2\pi\mu_0\Lambda_s$ is the vortex line energy, the effective $\tilde{\xi} \approx 0.34\xi_s$ accounts for the vortex core energy, and J_s is a uniform sheet current density. The maximum in $E(x)$ occurs at $x = x_m$, where:

$$x_m = \frac{w}{\pi} \cot^{-1} \frac{J_s}{J_0}, \quad J_0 = \frac{\pi\epsilon}{\phi_0 w} = \frac{\phi_0}{2\mu_0 w \Lambda_s} \sim \frac{\xi_s}{w} J_d \ll J_d \quad (\text{S12})$$

The London model with a point vortex core is applicable for a wide strip with $w \sim (10^2 - 10^3)\xi_s$, but becomes invalid for a vortex spaced by $\sim \xi_s$ from the edges. Here $E(x)$ given by Eq. (S11) diverges logarithmically at $x \rightarrow 0$, whereas the energy of a vortex emerging from the strip edge vanishes. Numerical calculations of $E(x)$ using the Ginzburg-Landau equations [2] have shown that the London model describes $E(x_m)$ well if J_s is not too close to J_d , and the energy barrier at $J_s = J_d$ vanishes. To take this effect into account, we define the energy barrier for the vortex entry as $U = E[x_m(J)] - E[x_m(J_d)]$, where $E(x)$ and x_m are given by Eq. (S11) and (S12). At $J_s \gg J_0$ this yields the energy barrier independent of the film width:

$$U = \epsilon \ln(J_d/J_s), \quad J_s \gg J_d \xi / w. \quad (\text{S13})$$

This gives a reasonable estimate of $U(J)$ at $J_s \simeq J_d$ at which $x_m \sim \xi_s \ll w$ shifts close to the edge of the film, as depicted in Fig. S3. Thermally-activated hopping of vortices over the edge barrier results in a mean dc voltage $V = V_0 (J_s/J_d)^{\epsilon/T}$, where V_0 was evaluated in [1]. At $\epsilon/T \gg 1$ and $J_s \simeq J_d$ the V-I curve takes the form:

$$V = V_0 \exp[-U/T], \quad U \simeq \epsilon(1 - J_s/J_d). \quad (\text{S14})$$

For our 3 nm thick WSi films with $\lambda = 950$ nm and $\Lambda \approx 600 \mu\text{m}$, we get $\epsilon \simeq 66$ K. At $J_s = 0.9J_d$ and $T = 0.9$ K the probability of thermally-activated penetration of a vortex from an ideal film edge is proportional to the small Arrhenius factor $\propto \exp(-U/T) \sim 7 \cdot 10^{-4}$ which can increase substantially due to edge defects which locally reduce the energy barrier and facilitate penetration of vortices. Edge defects can be small indentations or other microstructural features causing local variations of T_c or current crowding around defects. For instance, the local current density at the edge of a semicircular indentation of radius $R \gg \xi$ is twice the mean J_s , and larger concentration of impurities at the edges causes local reduction of J_d . Such defects serve as gates for local penetration of vortices for which the energy barrier $U(J_s)$ vanishes at the mean current density \bar{J}_d smaller than the bulk J_d . Given many material

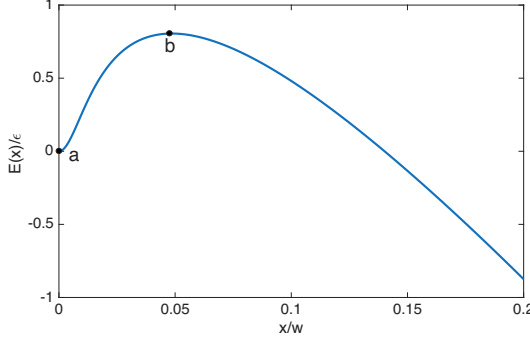


Fig. S3 Qualitative dependence of $E(x)$ on the vortex position evaluated from Eqs. (S1) regularized by $x \rightarrow \tilde{x} = [x^2 + \tilde{\xi}^2]^{1/2}$, $E(x) \rightarrow E(\tilde{x}) + \phi_0 J_s \tilde{\xi}$, $\tilde{\xi} = 10^{-2}w$ and $J_s = 20J_0$.

uncertainties depending on the film growth and deposition parameters, we assume that edge imperfections locally reduce the mean depairing density to $\tilde{J}_d < J_d$ in a narrow strip along the edges. It is the reduction of \tilde{J}_d at the edge which is mitigated by the current rails. With that in mind, consider now the number S_e of thermally-activated vortices penetrating over the edge barrier per unit time in a film of length L :

$$S_e = S_{e0} \exp \left[-\frac{\epsilon}{T} \left(1 - \frac{J_s}{\tilde{J}_d} \right) \right], \quad S_{e0} \sim \frac{L\nu}{l_i} \quad (\text{S15})$$

Here L/l_i is a number of statistically-independent vortex entries through edge defects with a mean spacing l_i and ν is an attempt frequency. In the overdamped limit characteristic of Abrikosov vortices, $\nu \simeq \sqrt{k_a k_b}/4\pi\eta$ follows from the classical result of Kramers [3], where k_a and k_b are curvatures of $E(x)$ at the bottom and the top of the potential well depicted in Fig. S3, $\eta = \phi_0^2 d_s / 2\pi \xi^2 \rho_n$ is the Mattis-Bardeen vortex drag coefficient, and ρ_n is the normal state resistivity. Taking $\sqrt{k_a k_b} \sim \phi_0^2 d_s / 4\pi \mu_0 \lambda_s^2 \xi^2$ at $J_s \sim \tilde{J}_d$ in Eq. (S15) yields

$$S_{e0} \sim \frac{L \rho_n}{8\pi \mu_0 \lambda_s^2 l_i} \quad (\text{S16})$$

For a WSi film with $L = 0.1$ mm, $\lambda = 950$ nm, $\rho_n = 2.5 \mu\Omega\text{m}$ and $l_i \sim 10^2$ nm, we get $S_{e0} \sim 10^{12} \text{ s}^{-1}$. Here Eq. (S6) is a rough, order of magnitude estimate which takes into account neither microstructural details of edge imperfections nor deformation of the vortex core at the edge in the presence of current [2]. The latter can result an extra factor $(1 - J_s/J_d)^n$ with $n = 1 - 2$, yet the logarithmic slope

$$\frac{d \ln S_e}{d J_s} = \frac{\epsilon}{T \tilde{J}_d} \quad (\text{S17})$$

is practically insensitive to uncertainties in S_{e0} and its possible power-law dependence on J_s if $T \ll \epsilon$.

From Eq. (S15), we obtain a maximum current I_{c1} which SSPD can carry at a given dark count rate S_c :

$$I_{c1} = \tilde{I}_d \left(1 - \frac{T}{\epsilon} \ln \frac{S_{e0}}{S_c} \right) \quad (\text{S18})$$

For $S_c = 10^2 \text{ s}^{-1}$ used in our definition of I_{sw} , $S_{e0} = 10^{12} \text{ s}^{-1}$, $\epsilon = 66 \text{ K}$, and $T = 0.9 \text{ K}$, we get $I_{c1} \approx 0.69 \tilde{I}_d$, where $\tilde{I}_d = w \tilde{J}_d$. Such operational I_{c1} equivalent to I_{sw} is limited by the acceptable dark count rate S_c and decreases logarithmically with the SSPD length. The account of the extra factor $(1 - J_s / \tilde{J}_d)$ in S_{e0} only increases I_{c1} by 3% and is neglected hereafter.

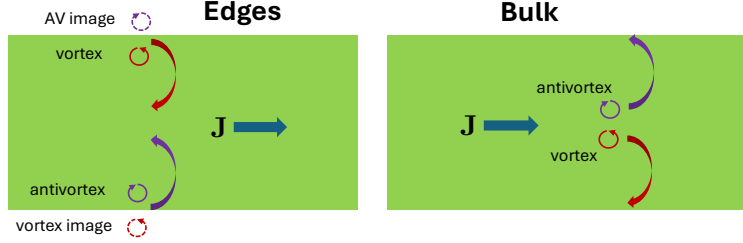


Fig. S4 Single vortices and antivortices penetrating from the film edges and vortex-antivortex pair unbinding inside the film due to thermal fluctuations.

Consider now the critical current I_{c2} limited by thermally-activated unbinding of VAV pairs inside the film. This process is illustrated in Fig. S4, from which it follows that the energy scale for the VAV pair production is twice that of the vortices penetrating from the edges:

$$U = 2\epsilon \left(1 - \frac{J_s}{J_d} \right), \quad J_s \sim J_d \quad (\text{S19})$$

This barrier vanishes at the bulk J_d larger than \tilde{J}_c for penetration of vortices from the edges. The VAV production rate in a film at $J_s \sim J_d$ can be evaluated in the same way as it was done above:

$$S_b = S_{b0} \exp \left[-\frac{2\epsilon}{T} \left(1 - \frac{J_s}{J_d} \right) \right], \quad S_{b0} \sim \frac{A\nu}{2\pi\xi_s^2}. \quad (\text{S20})$$

Here $A/2\pi\xi_s^2$ is a number of statistically-independent positions of the vortex core of size ξ_s in a film of area A and

$$S_{b0} \sim \frac{A\rho_n}{16\pi^2\mu_0\lambda_s^2\xi_s^2}. \quad (\text{S21})$$

The critical current limited by the bulk VAV pair production is then

$$I_{c2} = I_d \left(1 - \frac{T}{2\epsilon} \ln \frac{S_{b0}}{S_c} \right) \quad (\text{S22})$$

For $A = 20 \mu\text{m} \times 100 \mu\text{m}$, $\rho_n = 2.5 \mu\Omega\text{m}$, $\lambda_s = 950 \text{ nm}$, $\xi_s = 10 \text{ nm}$, $\epsilon = 66 \text{ K}$, and $T = 0.9 \text{ K}$, Eqs. (S21) and (S22) give $S_{b0} \sim 3 \cdot 10^{17} \text{ s}^{-1}$ and $I_{c2} \approx 0.76 I_d$ at $S_c = 10^2 \text{ s}^{-1}$. Here I_{c2} limited by the bulk VAV unbinding decreases logarithmically with the SSPD area.

As follows from Eqs. (S17) and (S22), the logarithmic slopes of dark count rates for the VAV pair unbinding and the vortex hopping from the edges are related by:

$$\frac{d \ln S_b}{dI} = \left(\frac{2\tilde{J}_d}{J_d} \right) \frac{d \ln S_e}{dI}. \quad (\text{S23})$$

According to our experimental data shown in Fig. 1(d) in the main text, the slope $d \ln S_b / dI$ abruptly increases by a factor 1.76 above a threshold current in the rails. This indicates switching from the dark counts limited by penetration of vortices from the edges to the bulk VAV pair unbinding. In this case Eq. (S23) can be used to evaluate the extent by which lithographic defects reduce the mean depairing current density at the edges: $\tilde{J}_d = 0.88 J_d$. Such relatively small decrease in \tilde{J}_d is in line with the magnitude of reduction of $J(x)$ at the edges obtained in our numerical results shown in Fig. S2(a).

References

- [1] Gurevich, A. & Vinokur, V. Size effects in the nonlinear resistance and flux creep in a virtual berezinskii-kosterlitz-thouless state of superconducting films. *Physical Review Letters* **100**, 227007 (2008).
- [2] Vodolazov, D. Saddle point states in two-dimensional superconducting films biased near the depairing current. *Physical Review B* **85**, 174507 (2012).
- [3] Hänggi, P., Talkner, P. & Borkovec, M. Reaction-rate theory: fifty years after kramers. *Reviews of Modern Physics* **62**, 251 (1990).